Inorganic Chemistry
Article
pubs.acs.org/IC

Role of Acentric Displacements on the Crystal Structure and Second-Harmonic Generating Properties of $RbPbCO_3F$ and $CsPbCO_3F$

T. Thao Tran,[†] P. Shiv Halasyamani,*[,†] and James M. Rondinelli*[,‡]

[†]Department of Chemistry, University of Houston, 112 Fleming Building, Houston, Texas 77204-5003, United States

[‡]Department of Materials Science & Engineering, Drexel University, 3141 Chestnut Street, Philadelphia, Pennsylvania 19104, United States

Ⓢ *Supporting Information*

ABSTRACT: Two lead fluorocarbonates, $RbPbCO_3F$ and $CsPbCO_3F$, were synthesized and characterized. The materials were synthesized through solvothermal and conventional solid-state techniques. $RbPbCO_3F$ and $CsPbCO_3F$ were structurally characterized by single-crystal X-ray diffraction and exhibit three-dimensional (3D) crystal structures consisting of corner-shared PbO_6F_2 polyhedra. For $RbPbCO_3F$, infrared and ultraviolet−visible spectroscopy and thermogravimetric and differential thermal analysis measurements were performed. $RbPbCO_3F$ is a new noncentrosymmetric material and crystallizes in the *achiral* and *nonpolar* space group $P\bar{6}m2$ (crystal class $\bar{6}m2$). Powder second-harmonic generation (SHG) measurements on $RbPbCO_3F$ and $CsPbCO_3F$ using 1064 nm radiation revealed an SHG efficiency of approximately 250 and 300 × α-SiO_2, respectively. Charge constants d_{33} of approximately 72 and 94 pm/V were obtained for $RbPbCO_3F$ and $CsPbCO_3F$, respectively, through converse piezoelectric measurements. Electronic structure calculations indicate that the nonlinear optical response originates from the distorted PbO_6F_2 polyhedra, because of the even−odd parity mixing of the O 2*p* states with the nearly spherically symmetric 6*s* electrons of Pb^{2+}. The degree of inversion symmetry breaking is quantified using a mode-polarization vector analysis and is correlated with cation size mismatch, from which it is possible to deduce the acentric properties of 3D alkali-metal fluorocarbonates.

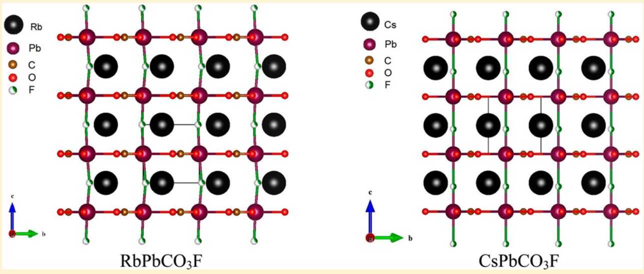

$RbPbCO_3F$ $CsPbCO_3F$

■ INTRODUCTION

Noncentrosymmetric (NCS) materials, that is, compounds that do not possess a crystallographic inversion center, are of technological interest owing to their functional ferroelectric, pyroelectric, piezoelectric, nonlinear optical (NLO), and multiferroic behaviors.[1−9] The design and synthesis of NCS materials remains an ongoing challenge as competing bonding forces often result in centrosymmetric structures. Nonetheless, a number of design strategies toward the creation of new NCS materials have been reported.[1−3,6,10−35]

We have focused on designing new NCS compounds[36−43] by using cations susceptible to second-order Jahn−Teller (SOJT) distortion: octahedrally coordinated d^0 transition-metal cations and lone-pair cations.[44−47] To achieve and enhance acentric polyhedra and inversion symmetry lifting distortions in crystalline materials, anionic substitution was developed.[48] Because fluoride carbonates constructed from $[(CO_3)_xF_y]^{n-}$ polyhedra are known to naturally occur in minerals,[49] they have garnered considerable attention owing to accessible hydrothermal synthetic methods. Second-harmonic generation (SHG) has been observed in rare-earth fluorocarbonates $Na_8Lu_2(CO_3)_6F_2$ and $Na_3Lu(CO_3)_2F_2$, with efficiency of approximately 4 × potassium dihydrogen phosphate (KDP) (160 × α-SiO_2).[50] Also, a series of alkaline−alkaline-earth fluorocarbonates, $ABCO_3F$ (A = K, Rb, Cs; B = Ca, Sr, Ba), was reported to be SHG active.[51] These two families of materials have a wide transparency range between 200 and 800 nm.[50,51] In addition, several centrosymmetric (CS) fluorocarbonates have been discovered, including $NaYbCO_3F_2$, $Na_2Yb(CO_3)_2F$, $Na_2EuCO_3F_3$, $Na_3La_2(CO_3)_4F$,[52−58] $BaMCO_3F_2$ (where M = Mn, Cu, and Zn),[56,57] and $Ba_2Co(CO_3)_2F_2$.[58]

Recently, we reported the synthesis and characterization of two new fluorocarbonates that incorporate a lone-pair cation—CS $KPb_2(CO_3)_2F$ and NCS $K_{2.70}Pb_{5.15}(CO_3)_5F_3$.[59] These materials exhibit the inherently asymmetric building blocks $Pb(CO_3)_3F$ and $Pb(CO_3)_3F_2$, which may be linked to create optically functional new NCS materials. Additional investigation in the alkali-metal−lead−fluorocarbonate family resulted in the discovery of two NCS materials—$RbPbCO_3F$ and $CsPbCO_3F$. $CsPbCO_3F$ was recently reported,[60] and it was suggested that the p−π interaction between Pb^{2+} and CO_3^{2-} is responsible for the large SHG response of 13.4 × KDP (530 × α-SiO_2). Remarkably, it was reported that Pb^{2+} is stereochemically *inactive*, and model electronic structure calculations on molecular $PbCO_3$ units identified enhanced *covalent* interactions at the origin of the SHG response upon inspection of

Received: April 2, 2014
Published: May 27, 2014

the real space extent of the molecular orbitals characterizing the highest occupied and lowest unoccupied states.

In this Paper, we report the synthesis, crystal structure, characterization, and atomic scale acentric property relationships of $RbPbCO_3F$ and $CsPbCO_3F$. The second harmonic response and piezoelectric coefficients are determined and correlated to the locally polar PbO_6F_2 units with the oxygen ligands associated with the cooperatively aligned triangular carbonate units. We disentangle the contribution of the acentric displacements in the achiral and nonpolar structures from the proposed electronic polarizability mechanisms using a scheme proposed by Wu et al.[11] and validated by Cammarata et al.[61] In this regard, recent applications of group representation theory and mode crystallography inspired by Chen's anionic group theory are applied in combination with density functional calculations that treat on equaling footing the point and translation periodicity of the system to address the microscopic origin for the NLO behavior. We find that the local Pb coordination environment is acentric and that the ionic−covalent balance among bridging ligands is highly anisotropic, suggesting that analysis of charge-density contours may be insufficient to deduce Pb^{2+} lone pair inactivity. Rather, the application of a mode-polarization analysis and quantitative evaluation of dynamical charges provides an improved structural descriptor of the SHG response, which opens a path to understand the acentric properties of other known three-dimensional (3D) fluorocarbonates.

■ EXPERIMENTAL SECTION

Reagents. RbF, CsF (Alfa Aesar, 99.5%), $Pb(OAc)_2{\cdot}3H_2O$, PbF_2, $PbCO_3$ (Sigma-Aldrich, 99.9%), MeOH (Sigma-Aldrich, 99%), and CF_3COOH (Sigma-Aldrich, 99%) were used as starting materials.

Synthesis. Crystals of $RbPbCO_3F$ and $CsPbCO_3F$ were grown by solvothermal techniques using a mixture of methanol and trifluoroacetic acid as a solvent. For $RbPbCO_3F$, the reaction mixture of 0.379 g (1.00×10^{-3} mol) of $Pb(OAc)_2{\cdot}3H_2O$, 0.627 g (6.00×10^{-3} mol) of RbF, 1.00 mL (2.47×10^{-2} mol) of methanol, and 1.00 mL (1.29×10^{-2} mol) of trifluoroacetic acid were placed in a 23 mL Teflon-lined stainless steel autoclave. The autoclave was closed, gradually heated up to 180 °C, held for 24 h, and then slowly cooled to room temperature at a rate of 6 °C h^{-1}. The solid products were isolated from the mother liquor by vacuum filtration and washed with ethanol. Under the same conditions, crystals of $CsPbCO_3F$ were grown separately by using 0.379 g (1.00×10^{-3} mol) of $Pb(OAc)_2{\cdot}3H_2O$, 0.608 g (4.00×10^{-3} mol) of CsF, 1.25 mL (3.09×10^{-2} mol) of methanol, and 1.25 mL (1.61×10^{-2} mol) of trifluoroacetic acid. Colorless trigonal prism-shaped crystals, subsequently determined to be $RbPbCO_3F$ and $CsPbCO_3F$, were obtained in approximately 60% and 70% yields, respectively, based on $Pb(OAc)_2{\cdot}3H_2O$. The reported compounds are slightly hygroscopic; thus, the products were stored in a vacuum desiccator.

Polycrystalline $RbPbCO_3F$ and $CsPbCO_3F$ were synthesized by conventional solid-state techniques. For $RbPbCO_3F$, stoichiometric amounts of dried RbF (0.418g, 4.00×10^{-3} mol) and $PbCO_3$ (1.07g, 4.00×10^{-3} mol) were thoroughly ground and pressed into a pellet. The pellet was placed in an alumina boat that was heated to 280 °C in flowing CO_2 gas, held for 3 d, and then cooled to room temperature at a programmed rate of 180 °C h^{-1}. For $CsPbCO_3F$, stoichiometric amounts of dried CsF (0.608g, 4.00×10^{-3} mol) and $PbCO_3$ (1.07g, 4.00×10^{-3} mol) were thoroughly ground and pressed into a pellet. The pellet was placed in an alumina boat that was heated to 270 °C in flowing CO_2 gas, held for 3 d, and then cooled to room temperature at a programmed rate of 180 °C h^{-1}. The materials were determined to be pure by powder X-ray diffraction (Supporting Information, Figure S1).

Single-Crystal X-ray Diffraction. A colorless trigonal prism crystal ($0.20 \times 0.12 \times 0.12$ mm^3) and a colorless plate-shaped crystal ($0.20 \times 0.12 \times 0.08$ mm^3) were selected for single-crystal diffraction analysis. Data were collected on a Bruker DUO platform diffractometer equipped with a 4K CCD APEX II detector using graphite-monochromated Mo Kα radiation. As $RbPbCO_3F$ and $CsPbCO_3F$ are slightly sensitive to moisture, single-crystal diffraction analyses were performed at a moderately low temperature, 213(2) K, utilizing liquid nitrogen. For each sample, a hemisphere of data (1519 frames at 6 cm detector distance) was collected using a narrow-frame algorithm with scan widths of 0.30° in ω and an exposure time of 35 s per frame. $RbPbCO_3F$ and $CsPbCO_3F$ crystals were found to have slight nonmerohedral and merohedral twinning, respectively. This minor twinning did not impact the subsequent solution and refinements. Data were integrated using the Bruker-Nonius SAINT program,[62] with the intensities corrected for Lorentz factor, polarization, air absorption, and absorption attributable to the variation in the path length through the detector faceplate. An empirical absorption correction was applied based on the entire data set. Redundant reflections were averaged. The positions of the lead atoms were determined by direct methods using SHELXS-97,[63] and the remaining atoms were located by difference Fourier maps and least-squares cycles, utilizing SHELXL-97.[64] All calculations were performed using the WinGX-98 crystallographic software package.[65] Relevant crystallographic data for $RbPbCO_3F$ and $CsPbCO_3F$ are given in Table 1. Selected bond distances and angles, atomic coordinates, and equivalent isotropic displacement parameters were deposited in the Supporting Information (Tables S1−S3).

Table 1. Crystallographic Data

	$RbPbCO_3F$	$CsPbCO_3F$
M (g mol^{-1})	371.67	419.11
T (K)	213(2)	213(2)
λ (Å)	0.710 73	0.710 73
crystal system	hexagonal	hexagonal
space group	$P\bar{6}m2$ (No. 187)	$P\bar{6}m2$ (No. 187)
a (Å)	5.3488(12)	5.393(3)
b (Å)	5.3488(12)	5.393(3)
c (Å)	4.8269(12)	5.116(2)
α (deg)	90	90
β (deg)	90	90
γ (deg)	120	120
V ($Å^3$)	119.59(5)	128.85(10)
Z	1	1
D_c (gcm^{-3})	5.161	5.401
μ (mm^{-1})	45.287	39.611
$2\theta_{max}$ (deg)	54.84	56.34
R_{int}	0.0201	0.0328
GOF	1.267	1.230
$R(F)^a$	0.0112	0.0191
$R_w(F_o^2)^b$	0.0258	0.0517
flack parameter	0.09(3)	0.32(2)
largest diff. peak/hole (e $Å^{-3}$)	0.673/−0.853	0.966/−0.680

$^aR(F) = \Sigma||F_o| - |F_c||/\Sigma|F_o|$. $^bR_w(F_o^2) = [\Sigma w(F_o^2 - F_c^2)^2/\Sigma w(F_o^2)^2]^{1/2}$

Powder X-ray Diffraction. Powder X-ray diffraction (PXRD) measurements on $RbPbCO_3F$ and $CsPbCO_3F$ materials were performed using a PANalytical X'Pert PRO diffractometer equipped with Cu Kα radiation. Data were collected in the 2θ range of 5°−70° with a step size of 0.008° and a scan time of 0.3 s. No impurities were observed, and the experimental and calculated PXRD are in very good agreement (Supporting Information, Figure S1).

Infrared Spectroscopy. The Fourier transform infrared spectroscopy (FTIR) spectrum for $RbPbCO_3F$ was collected on a Bruker Tensor 37 FTIR with the use of a KBr pellet pressed at 15 000 PSI. A total of 64 scans were recorded, and a background spectrum was subtracted (Supporting Information, Figure S2).

UV−vis Diffuse Reflectance Spectroscopy. UV−visible (UV−vis) reflectance data of $RbPbCO_3F$ were collected on a Varian Cary 500 Scan UV−vis-NIR spectrophotometer over the 200−2000 nm spectral range at room temperature. Poly(tetrafluoroethylene) was used as a diffuse reflectance standard. The reflectance spectrum was converted to absorption using the Kubelka−Munk function (Supporting Information, Figure S3).[66,67]

Thermal Analysis. Thermogravimetric analyses were performed on an EXSTAR TG/DTA 6300 instrument. Approximately 20 mg of $RbPbCO_3F$ was placed separately in a platinum pan and heated at a rate of 10 °C min^{-1} from room temperature to 900 °C under flowing N_2 (Supporting Information, Figure S4).

Energy-Dispersive X-ray Spectroscopy Analysis. A JEOL JSM 6330F scanning electron microscope equipped with an electron dispersive spectrometer was used to determine the rubidium-to-lead ratio. The collected crystal of $RbPbCO_3F$ was mounted on one flat face and coated with 25 nm thickness carbon. Intensity data were processed by Oxford IsisLink software. Standards used were $RbAlSi_3O_8$ for rubidium and $PbCrO_4$ for lead. Three analyses on this sample were obtained with a focused beam of 15 keV of accelerating voltage and 12 μA of emission current, one on each of the three visible faces.

Second-Harmonic Generation (SHG). Powder SHG measurements were performed on a modified Kurtz nonlinear optical (NLO) system using a pulsed Nd:YAG laser with a wavelength of 1064 nm. A detailed description of the equipment and methodology has been published.[68] As the powder SHG efficiency has been shown to strongly depend on particle size,[69] $RbPbCO_3F$ and $CsPbCO_3F$ were ground and sieved into distinct particle size ranges (<20, 20−45, 45−63, 63−75, 75−90, >90 μm). Relevant comparisons with known SHG materials were made by grinding and sieving crystalline α-SiO_2 and $LiNbO_3$ into the same particle size ranges. No index-matching fluid was used in any of the experiments.

Piezoelectric Measurements. Converse piezoelectric measurements were performed using a Radiant Technologies RT66A piezoelectric test system with a TREK (model 609 × 10^{-6}) high-voltage amplifier, Precision Materials Analyzer, Precision High Voltage Interface, and MTI 2000 Fotonic Sensor. $RbPbCO_3F$ and $CsPbCO_3F$ were pressed into pellets (∼1.2 cm diameter, ∼0.7 mm thickness) and sintered at 260 °C for 3 d. Silver paste was applied to both sides of the pellet, and the pellet was cured at 250 °C for 12 h. For all of the structural figures, the program VESTA was used.[70]

Electronic Structure Calculations. First-principles density functional theory (DFT) calculations were carried out using the Vienna *ab initio* Simulation Package[71,72] (VASP) within the PBEsol[73] generalized-gradient approximation with a planewave cutoff of 540 eV. The projector augmented-wave (PAW) method[74] was used to treat the interaction between the core and valence electrons with pseudopotentials constructed with the following valence configurations: $5s^25p^66s^1$ (Cs), $4s^24p^65s^1$ (Rb), $6s^26p^2$ (Pb), $2s^22p^2$ (C), $2s^22p^4$ (O), and $2s^22p^5$ (F). In all calculations an 8 × 8 × 8 Γ-centered *k*-point mesh and the linear tetrahedron method with Blöchl corrections[75] was applied for sampling and Brillouin zone integrations, respectively. All DFT calculations were performed on ordered fluorine structural variants (100% occupancy) with an averaged atomic position (2/3,1/3,0) for $RbPbCO_3F$ and (0,0,1/2) for $CsPbCO_3F$.

■ RESULTS

Structures. $RbPbCO_3F$ exhibits a 3D crystal structure consisting of corner-sharing $Pb(CO_3)_3F_2$ polyhedra (see Figure 1). The Pb^{2+} cations are connected to carbonate groups in the *ab*-plane, and along the *c*-axial direction the connectivity is through bridging fluorides. The Rb^+ cations are located in the cavities formed between $Pb(CO_3)_3F_2$ polyhedral building units. In this structure model, the bridging fluorine is observed to be statistically disordered in the *ab*-plane, resulting in a Pb−F−Pb angle of 170.8(9)°. In connectivity terms, the material may be written as $[Pb(CO_3)_{3/3}F_{2/2}]^{1-}$, with charge balance maintained by one Rb^+ cation. Each Pb^{2+} cation is bonded to six oxygen atoms and two fluorine atoms in a distorted hexagonal bipyramidal coordination environment, with Pb−O distances of 2.6864(8) Å and Pb−F distances of 2.421(7) Å. The carbonate C−O distance is 1.290(6) Å. The Rb^+ cation is surrounded by six oxygen atoms and three fluorine atoms, with Rb−O distances of 3.010(3) Å and Rb−F distances of 3.00(4) Å. Bond valence calculations resulted in values of 1.11, 1.97, and 3.93 for Rb^+, Pb^{2+}, and C^{4+}, respectively (Supporting Information, Table S4).[76,77] The anisotropic displacement parameters of $RbPbCO_3F$ are depicted in Figure 2 as ellipsoid diagrams.

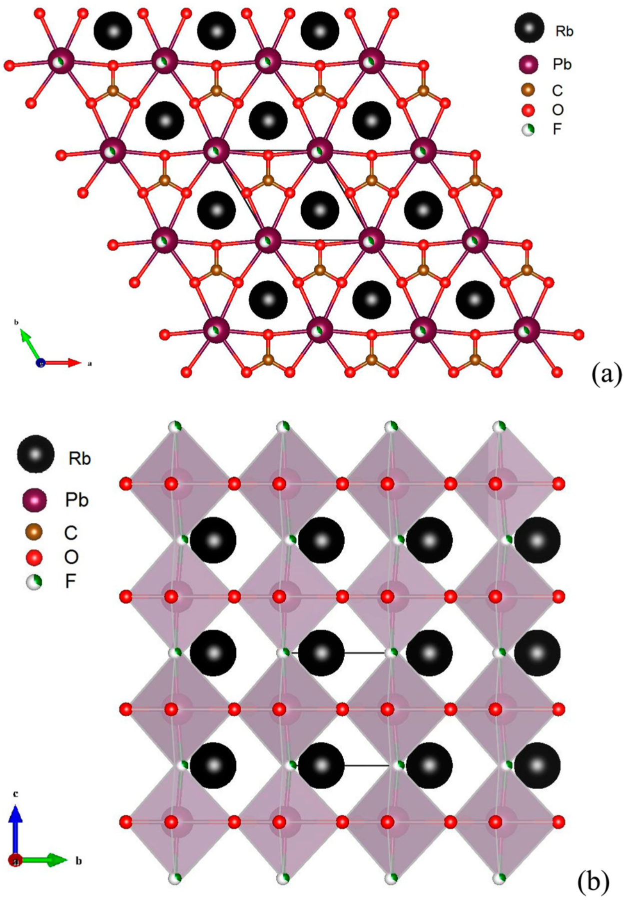

Figure 1. Representations of $RbPbCO_3F$. (a) Ball-and-stick model in the *ab*-plane. (b) Polyhedral model in the *bc*-plane. Only one position of the disordered bridging fluoride in the structure is shown.

For $CsPbCO_3F$, we noted discrepancies between our structure and the recently reported one during our data collection and refinement. In the reported structure, the bridging fluoride was entirely ordered in a $\overline{6}m2$ crystallographic site, resulting in a symmetric bridge having identical Pb−F distances of 2.5536(7) Å.[60] Also, the equivalent isotropic displacement U_{eq} for F was significantly greater than those for other atoms.[60] In addition, the bond valence sum value of Pb^{2+} was reported to be 1.686, which can be considered to be fairly under-bonded.[60] Our data clearly reveal that the bridging F atom is statistically disordered along the *c*-axis direction. The thermal displacement parameters of our structure refinement are represented in Figure 2.

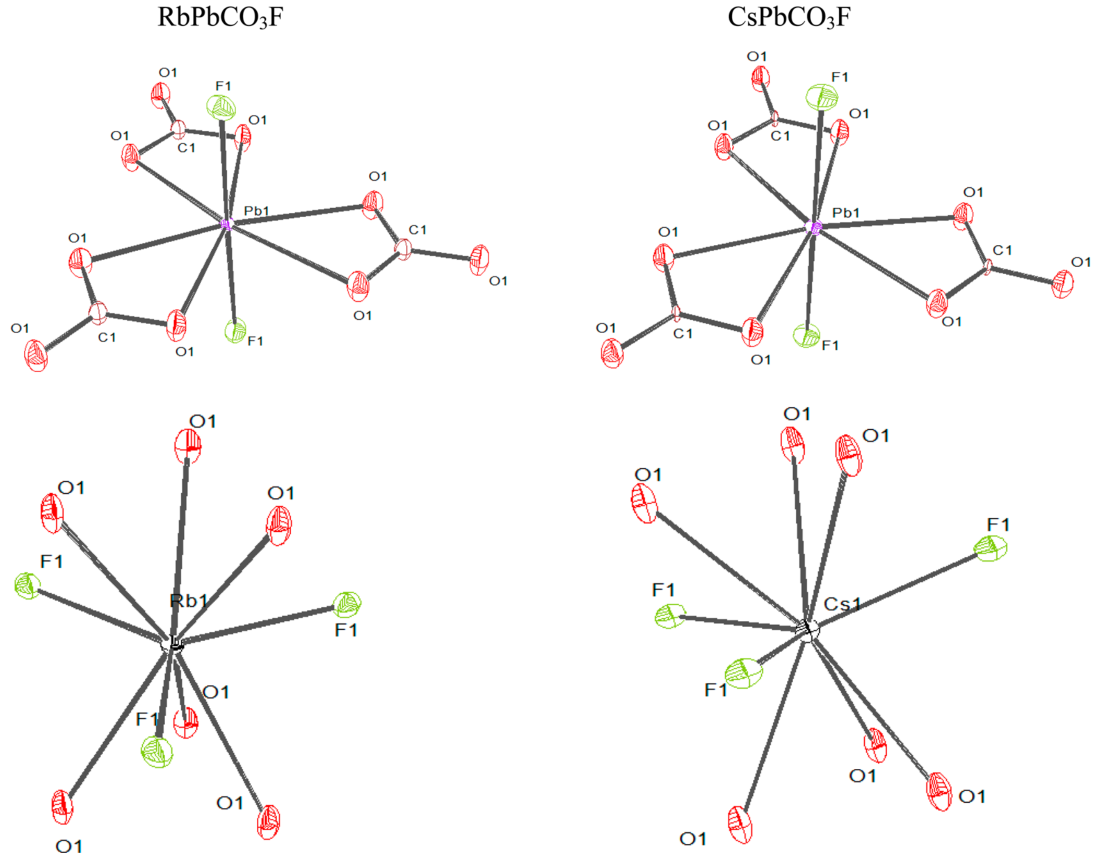

Figure 2. ORTEP (50% probability ellipsoids) diagrams of $RbPbCO_3F$ and $CsPbCO_3F$. Note that the F atoms, which were refined to be disordered, have well-behaved thermal parameters.

Similar to $RbPbCO_3F$, $CsPbCO_3F$ also exhibits a 3D structure consisting of corner-sharing $Pb(CO_3)_3F_2$ polyhedra (see Figure 3). The Pb^{2+} cations are connected by carbonate groups in the *ab*-plane, and along the *c*-axis direction the connectivity is through a bridging fluoride. The Cs^+ cations are located in cavities formed between $Pb(CO_3)_3F_2$ polyhedral building units. The static disorder of the bridging fluoride along the *c*-axis direction results in a shorter and a longer Pb−F distance. The Pb^{2+} cation is observed in a distorted hexagonal bipyramidal environment, with Pb−O distances of 2.709(2) Å and Pb−F distances of 2.23(3) and 2.88(3) Å. In connectivity terms, the material may be written as $[Pb(CO_3)_{3/3}F_{2/2}]^{1-}$, with charge balance maintained by one Cs^+ cation. The Cs^+ cation is surrounded by six oxygen atoms and three fluorine atoms, with Cs−O distances of 3.136(7) Å and Cs−F distances of 3.131(3) Å. Bond valence calculations resulted in values of 1.20, 1.89, and 3.84 for Cs^+, Pb^{2+}, and C^{4+}, respectively (Supporting Information, Table S5).[76,77]

Infrared Spectroscopy. The IR spectrum of $RbPbCO_3F$ revealed C−O vibrations between 1400 and 680 cm^{-1}. The strong broad band observed at 1410 cm^{-1} can be assigned to the stretching C−O vibration. The out-of-plane vibration, δ(OCO), is observed in the range of 840−830 cm^{-1} as a medium band, and the bending vibration, δ(OCO), should appear between 700 and 670 cm^{-1} as a medium weak band.[78−81] A strong band, however, was observed in the range of 700−670 cm^{-1}, which can be attributed to the overlap between the bending vibration δ(OCO) and the stretching vibration ν(Pb−O).[80,81] The ν(Pb−F) vibration is observed at ~400 cm^{-1}.[81] The IR spectrum was deposited in the Supporting Information (Figure S2).

UV−vis Diffuse Reflectance Spectroscopy. The UV−vis diffuse reflectance spectrum revealed that the absorption energy for $RbPbCO_3F$ is approximately 4.1 eV (302 nm). This is consistent with the white color of the materials. Absorption (K/S) data were calculated from the Kubelka−Munk function.[66,67]

$$F(R) = \frac{(1-R)^2}{2R} = \frac{K}{S}$$

where R represents the reflectance, K represents the absorption coefficient, and S represents the scattering factor. The UV−vis diffuse reflectance spectrum was deposited in the Supporting Information (Figure S3).

Thermal Analysis. The thermal behavior of $RbPbCO_3F$ was investigated using thermogravimetric analysis (TGA) and differential thermal analysis (DTA) under N_2 atmosphere. The decomposition of material begins at approximately 300 °C, corresponding to the loss of CO_2. The experimental weight loss is in good agreement with the calculated weight loss. The endothermic peaks in the heating curve are consistent with the decomposition of the material. At approximately 755 °C, the drop in mass observed in the TGA plot is likely attributable to the loss of fluorides. The exothermic peaks in the cooling cycle indicate recrystallization of the residues of $RbPbCO_3F$ occurred at approximately 860 and 760 °C. That is confirmed by the appearance of two different modifications of lead(II) oxide, that is, PbO (*P*4/*nmm*) and PbO (*Pbcm*), in the powder XRD pattern of the residuals. The thermal behaviors of the decomposition products are consistent with those reported

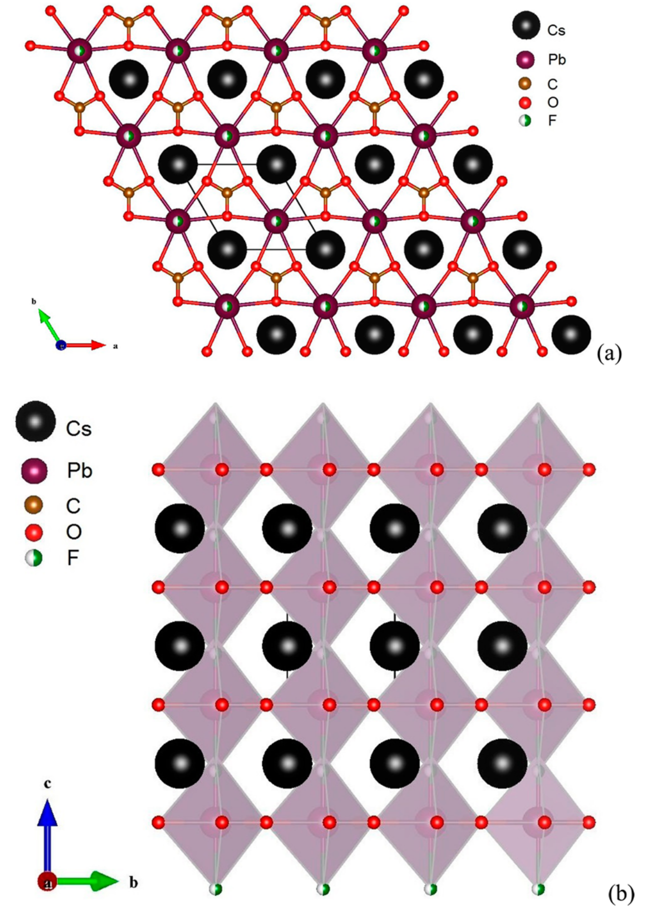

Figure 3. Representations of $CsPbCO_3F$. (a) Ball-and-stick model in the *ab*-plane. (b) Polyhedral model in the *bc*-plane. Only one position of the disordered bridging fluoride in the structure is shown.

previously.[82] The DTA/TGA diagrams and powder XRD spectra for $RbPbCO_3F$ were deposited in the Supporting Information (Figures S4 and S5).

Energy-Dispersive X-ray Spectroscopy Analysis. The semiquantitative energy-dispersive X-ray spectroscopy (EDS) measurements were taken three times from the selected $RbPbCO_3F$ crystal that was used for X-ray diffraction analysis. The average Rb/Pb ratio of 1.06(9) found by EDS is in excellent agreement with the value of 1.00 determined by least-squares refinement of the X-ray data.

Second-Harmonic Generation (SHG) and Piezoelectric Measurements. Since $RbPbCO_3F$ and CsPbCO3F crystallize in the NCS space group $P\bar{6}m2$, we investigated the SHG and piezoelectric properties. Powder SHG measurements using 1064 nm radiation revealed an SHG efficiency of approximately 250 and 300 × α-SiO_2, respectively, in the 45−63 μm particle size range. Additional SHG measurements, particle size versus SHG efficiency, indicate both materials exhibits type 1 phase-matching behavior. As such $RbPbCO_3F$ and $CsPbCO_3F$ fall into the class A category of SHG materials, as defined by Kurtz and Perry (see Figure 4).[83] On the basis of these measurements, we estimate an average NLO susceptibility $\langle d_{\mathrm{eff}}\rangle_{\mathrm{exp}}$ of approximately 17 pm/V and 20 pm/V for the Rb and Cs phases. Although estimating the average NLO susceptibility solely from powders tends to overestimate $\langle d_{\mathrm{eff}}\rangle_{\mathrm{exp}}$, our powder-SHG results for $CsPbCO_3F$ are consistent with those reported earlier.[60]

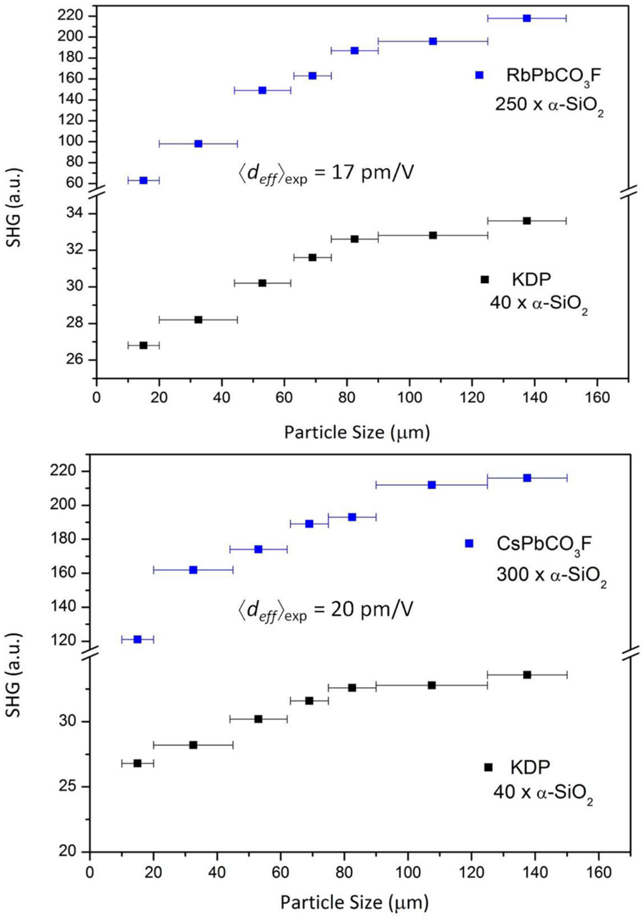

Figure 4. Powder second-harmonic generation for $RbPbCO_3F$ and $CsPbCO_3F$.

Converse piezoelectric measurements on $RbPbCO_3F$ and $CsPbCO_3F$ were also performed, and piezoelectric charge constants d_{33} of approximately 72 pm/V and 94 pm/V, respectively, were determined (see Figure 5).

Electronic Structure. Figure 6 shows the atom-resolved densities of states (DOS) for $RbPbCO_3F$ (upper panel) and $CsPbCO_3F$ (lower panel). First, we obtain a band gap of 3.18 and 3.31 eV for $RbPbCO_3F$ and $CsPbCO_3F$, respectively, (at the DFT-PBEsol level), consistent with the concept that Cs expands the lattice and makes the compound more ionic. The two-photon electronic excitation involved in SHG is between states across these gaps. Here we find that the onset of the valence band (VB) edge is sharper in $CsPbCO_3F$ and the bandwidth is much narrower (by 1 eV) compared to the $RbPbCO_3F$ material, which is consistent with the observed larger SHG response in the Cs compound over the Rb phase. In both structures the frontier orbitals in the VB are largely derived from the O 2p states of the $[CO_3]^{2-}$ group mixed with the nearly spherically symmetric 6s electrons of the Pb^{2+} cation; the low-lying states in the conduction band are mainly composed of the Pb 6p states. This electronic configuration is ideal for the electric field of an incident photon to produce an acentric and polarized charge distribution, because of the even−odd parity mixing of the states in the lowest unoccupied molecular orbital and highest occupied molecular orbital. The alkaline metal states are deep in the valence band (data not shown), centered at −9 eV (Pb) and ranging from −7 to −5 eV (Cs); therefore, they should not largely influence the optical

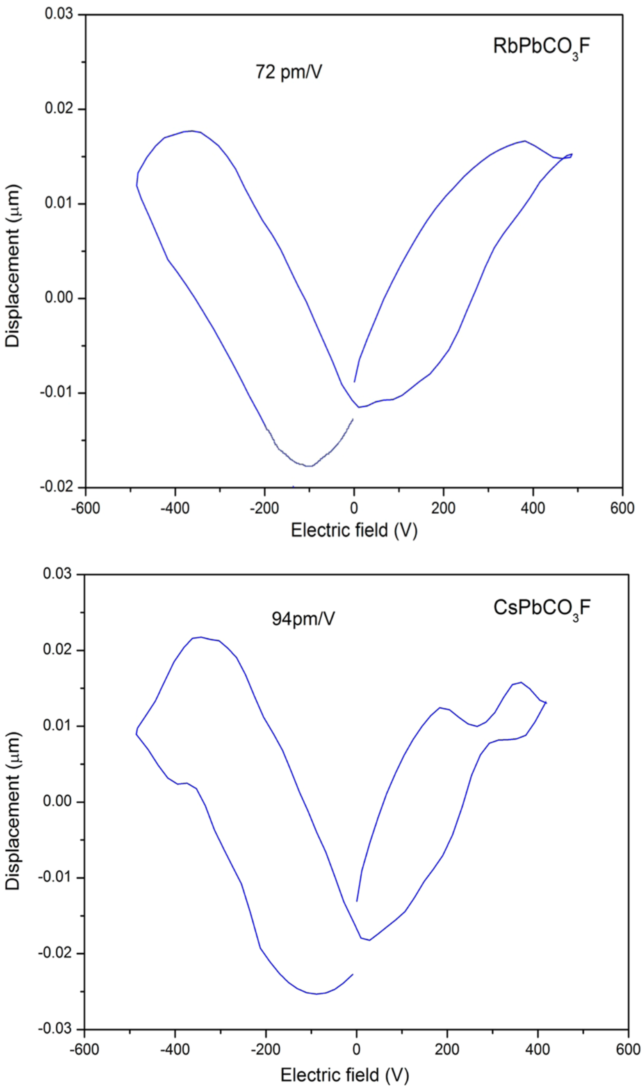

Figure 5. Displacement vs electric field loops for RbPbCO$_3$F and CsPbCO$_3$F.

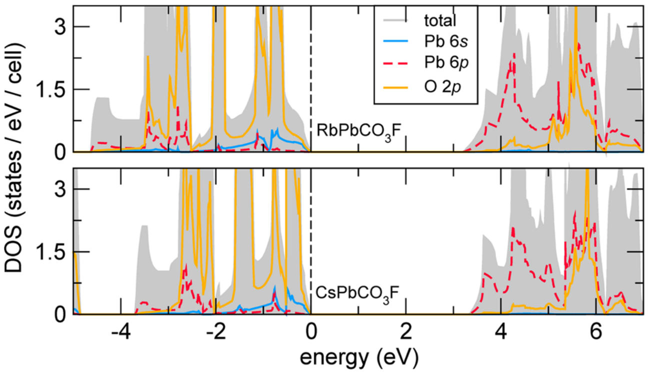

Figure 6. Electronic DOS for RbPbCO$_3$F and CsPbCO$_3$F decomposed by atomic site and orbital contributions.

transition. The role of these large metal cations is to provide the crystalline lattice topology for the packing of the SHG-active PbCO$_3$ groups, which we explore in more detail from a structural perspective below.

■ DISCUSSION

Structures. As discussed earlier, in the RbPbCO$_3$F structure, the statistical disorder of the bridging F atom in the *ab*-plane results in a Pb–F–Pb angle of 170.8(9)°. This specifically disordered fluorine was also observed in $K_{2.70}Pb_{5.15}(CO_3)_5F_3$ with a corresponding Pb–F–Pb angle of 169.5(16)°.[59] Note that in these materials, the Pb–F–Pb is symmetrically bridged with two identical Pb–F distances, and the disordered F renders a Pb–F–Pb angle offset by about 10° from 180°.

With respect to the CsPbCO$_3$F structure, the F atom was initially also refined on a $\overline{6}m2$ site (0,0,1/2) midway between Pb atoms, which created a symmetrically bridged linear chain along the *c*-axis. However, it was noted that U_{33}, the component of the anisotropic displacement along the *c* direction, was very large, which was also observed in the previously reported CsPbCO$_3$F structure.[60] The large U_{33} clearly indicated that the F atom was not actually on the $\overline{6}m2$ site, but instead was displaced by a significant distance, 0.32 Å, from this crystallographic site in a disordered arrangement. The *z*-coordinate parameter was allowed to refine independently rendering a converged value of 0.4360(4), and the anisotropic displacement parameters of the F atom is well-behaved (see Figure 2). Attributable to the disorder, shorter (2.23(3) Å) and longer (2.88(3) Å) Pb–F bonds are observed. These Pb–F bond lengths are consistent with those reported in literature.[84,85] As would be expected, the Pb–F distances in our structural model are different from the previous report,[60] where two Pb–F distances are 2.5536(7) Å. This distance is simply an average of the two true Pb–F distances and not an actual accurate bond distance. Also, in our model there is an improvement in bond valence sum for Pb^{2+} in our structure compared to the reported value, 1.89 versus 1.686.[60]

Further examination of the two related materials, RbPbCO$_3$F and CsPbCO$_3$F, reveals some similarities and differences in the crystallographic architecture. These materials both crystallize in the hexagonal $P\overline{6}m2$ space group with the *a* and *b* unit cell parameters nearly identical (5.3488(12) versus 5.393(3) Å for the Rb and Cs compounds, respectively) since the parameters are defined by the Pb(CO$_3$)$_3$ bonding patterns. The *c*-axes, however, are different (4.8269(12) (Rb) vs 5.116(2) Å (Cs)), and these are a function of the Pb–F distances associated with the size of the alkaline cation (see Figures 1 and 3). RbPbCO$_3$F and CsPbCO$_3$F are structurally similar and built up from the Pb(CO$_3$)$_3$F$_2$ building units. With respect to the "A" cations, the effective ionic radii are 1.63 and 1.78 Å for Rb$^+$ and Cs$^+$, respectively.[86] If we replace Rb$^+$ with the larger cation Cs$^+$ in the structure, we notice that the cavity separation is not very big. In other words, when the larger cation Cs$^+$ is introduced into the crystal structure, the structural strain is produced inside the cavities between the Pb(CO$_3$)$_3$F$_2$ frameworks. To minimize this strain, the Pb(CO$_3$)$_3$ layers need to slightly separate along the *c*-direction to accommodate the larger cation Cs$^+$. This phenomenon is clearly observed in the increase of the *c*-axis of unit cell parameters (see Table 1). The *c*-axis of CsPbCO$_3$F is longer than that of RbPbCO$_3$F, whereas the *a*- and *b*-axes remain essentially constant.

For fluorocarbonate materials, the spatial arrangement of the acentric carbonate groups with respect to the overall structure has been previously described.[87−89] It has been observed that in fluorocarbonates, the CO$_3$ group may be parallel or inclined with regard to the rest of the structure. The carbonate groups in

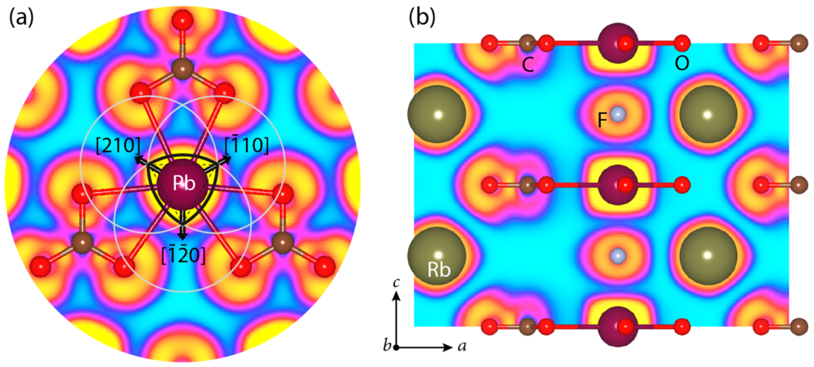

Figure 7. Reuleaux triangle projection overlaid on charge-density contours of the ELF in the (001) plane about the Pb site in $RbPbCO_3F$. ELF plot in the $(\bar{1}20)$ plane corresponding to a planar slice along the [210] direction intersecting the "vertex" of the Reuleaux triangle. The red, silver, brown, and maroon spheres correspond to oxygen, fluorine, carbon, and lead atoms, respectively.

$RbPbCO_3F$ and $CsPbCO_3F$ are parallel to the entire structures, which is similar to other 3D fluorocarbonates such as $KSrCO_3F$, $RbSrCO_3F$, and $KCaCO_3F$.[51] Along the *c*-axis, the eclipsed and staggered arrangements of the carbonate groups were observed in our $KPb_2(CO_3)_2F$ and $K_{2.70}Pb_{5.15}(CO_3)_5F_3$,[59] whereas the acentric CO_3 groups in Rb and Cs members of this family are found to align in a coplanar and coparallel fashion with respect to the overall structural architecture, which should produce a structural contribution to the observed SHG efficient.

In $RbPbCO_3F$ and $CsPbCO_3F$, the asymmetric coordination environments of the Pb^{2+} atoms are polar, that is, each PbO_6F_2 polyhedron exhibits a local dipole moment. Since the structures are composed of PbO_6F_2 polyhedra with equal polarization magnitudes but are aligned in opposite directions, the net dipole moments in these materials are zero. Therefore, the structures are macroscopically not polar.

Relationship between Lone Pair (In)activity, NCS Structures, and Acentric Crystal Properties. First, we examine in more detail the electronic structure and charge-density distribution by computing the electron localization function (ELF) for both $RbPbCO_3F$ and $CsPbCO_3F$ (Supporting Information, Figure S6). Consistent with ref 59, we find that there is an asymmetric electron density arranged about the oxygen atoms forming the carbonate group, which is repeated in a cloverlike pattern. Interestingly, the electronic density about the Pb^{2+} sites is nearly symmetric and resembles a Reuleaux (rounded equilateral) triangle[90] when viewed in projection (Figure 7a). The Pb cation is located at the center of the triangle, which is formed by the space shared by three equivalent circles, each of which has a center tangent to the other and is simultaneously collinear with the nearest-neighbor carbon atoms. As a result, the charge density on any side of the Pb cation remains equidistant to the opposite "vertex" of maximum density (arrowed) and thus may become highly polarizable along the Reuleaux triangle vertices, that is, in the $[\bar{1}10]$, [210], and $[\bar{1}10]$ directions upon excitation by the electric field of an incident photon.

Indeed, projection of the ELF plot along the normal to these directions reveals that charge density about the Pb^{2+} site is unevenly distributed in the plane (Figure 7b). The bloated electron density extends further along the positive *a* direction than it does along the negative *a* direction in the $(\bar{1}20)$ plane. This is evident by comparing the high electron-density regions about the Pb site with the Pb−O bond due to neighboring carbonate units. Interestingly, the electron localization about the fluorine anions is also highly anisotropic (Figure 7b), which manifests in our Born effective charges (Z^*) for fluorine (Supporting Information, Table S6). We find dynamical charges of $Z^*_{11} = -0.7$ and $Z^*_{33} = -3.3$, whereas the nominal ionic value is −1. The anomalous value for Z^*_{33} is indicative of an electric polarization to develop along the 6-fold axis since Z^* is the proportionality constant between the electric field and the force applied on the ion by the field. The reduced value in the basal plane suggests real-space charge transfer and more ionic character. Similar anomalous values are found for Pb^{2+} (Supporting Information, Table S6), albeit in the basal plane, owing to the strong dynamic charge transfer along the Pb−O bond linked with the carbonate groups consistent with ionic−covalent character of the fluorocarbonates. Thus, while in the ground state these fluorocarbonates may not present an obvious lobe of electron density corresponding to well-defined static lone-pair, the charge density about the Pb^{2+} is indeed asymmetric, and the excited state structure should display large Pb^{2+} lone-pair activity.

We next explore how the atomic structure supports the bonding interactions giving rise to these density distributions and use a structural approach to explain contributions to the acentric properties. We compute the total mode-distortion vector for each compound following the procedure described by Wu et al.[11] Note that we were unable to identify a pseudosymmetric centrosymmetric structure that obeyed constraints on integer stoichiometry attributable to Wyckoff site splitting; therefore, we perform the analysis using an idealized $P\bar{6}m2$ structure (Supporting Information, Table S7), while including the fractional site occupancies. We find the amplitude of the mode-polarization vectors to be 0.48 and 0.55 Å for $RbPbCO_3F$ and $CsPbCO_3F$, respectively, with the main atomic displacements connecting the idealized structures via distortions of the anionic network from oxygen and fluorine displacements in the *ab*-plane. Next, we obtain the specific acentric-mode displacements[11] (SAMD), which correspond to the normalized amplitude of the inversion lifting displacements described by the mode-polarization vector per unit cell volume. We find values of 4.03×10^{18} Å/cm^3 and 4.29×10^{18} Å/cm^3 in $RbPbCO_3F$ and $CsPbCO_3F$, respectively.

Consistent with the acentric mode displacement analysis, we find that the converse piezoelectric charge coefficients d_{33} for $RbPbCO_3F$ (72 pm/V) is lower than that of $CsPbCO_3F$ (94 pm/V). These values are larger than those observed in α-SiO_2 (2.3 pm/V),[91] $LiNbO_3$ (15 pm/V),[91] and $K_{2.70}Pb_{5.15}(CO_3)_5F_3$ (20 pm/V),[59] and are similar to those of $Ba_{1-x}La_xTi_{1-x}Cr_xO_3$

Table 2. Summary of A–M–CO_3–F (A = Na, K, Rb, or Cs) Compounds

	radius ratio of A^+/M^{n+}	structural dimension	centricity	space group	ref
$Na_3La_2(CO_3)_4F$	0.976	2	CS	$P6_3/mmc$	55
$NaLa_2(CO_3)_3F$	0.976	3	NCS	$P\bar{6}m2$	94
$Na_3Ce_2(CO_3)_4F$	0.992	2	CS	$P6_3/mmc$	89
$NaCe_2(CO_3)_3F$	0.992	3	NCS	$P\bar{6}m2$	94
$KPb_2(CO_3)_2F$	1.07	2	CS	$P6_3/mmc$	59
$K_{2.70}Pb_{5.15}(CO_3)_5F_3$	1.07	2	NCS	$P\bar{6}m2$	59
$NaYCO_3F_2$	1.09	3	CS	$Pmcn$	95
$NaYbCO_3F_2$	1.14	3	CS	$Pnma$	52
$KSrCO_3F$	1.23	3	NCS	$P\bar{6}m2$	51
$RbPbCO_3F$	1.26	3	NCS	$P\bar{6}m2$	this work
$RbSrCO_3F$	1.29	3	NCS	$P\bar{6}m2$	51
$KGdCO_3F_2$	1.36	3	CS	$Fddd$	96
$K_4Gd_2(CO_3)_3F_4$	1.36	3	NCS	$R32$	97
$CsPbCO_3F$	1.38	3	NCS	$P\bar{6}m2$	60 and this work
$KCaCO_3F$	1.38	3	NCS	$P\bar{6}m2$	51
$RbCaCO_3F$	1.54	3	NCS	$P\bar{6}m2$	51
$CsCaCO_3F$	1.68	3	NCS	$P\bar{6}m2$	51
$KCuCO_3F$	2.38	3	NCS	$Pmc2_1$	98

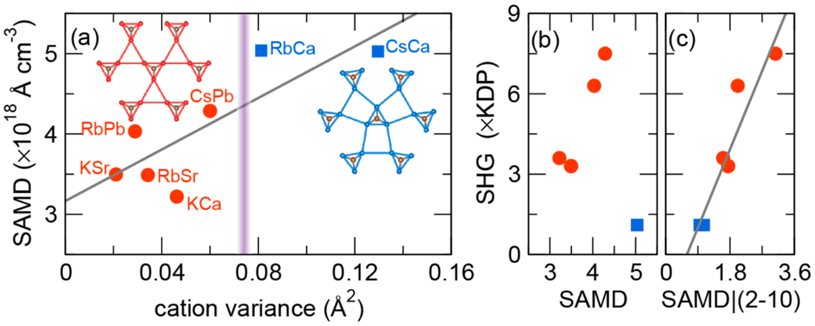

Figure 8. (a) Relationship between the alkali metal and divalent cations in 3D fluorocarbonates and the SAMD. All structures exhibit the D_{3h} point symmetry, with the different symbols (colors) corresponding to compounds with Z = 1 (●, red) or Z = 3 (■, blue) separated by a vertical bar (gradient). The gray line is a linear least-squares fit to the data (R = 0.82). Insets depict the $[CO_3]^{2-}$ topology, with other atoms omitted for clarity. SHG efficiency for the same compounds relative to (b) the total SAMD and (c) the reduced SAMD obtained from displacements on the $(2\bar{1}0)$ plane.

(70 pm/V)[92] and $(Bi_{0.5}Na_{0.5})_{0.95}Ba_{0.05}TiO_3$ (95 pm/V).[93] The structural origin of the piezoelectric behavior may also be attributable to the magnitude of the SAMD, because when the voltage is applied the sample undergoes macroscopic strain[68] that is mediated by strain-polarization coupling owing to the coparallel arrangement and constructive interaction of the electronically flexible carbonate units. The more total polarizability the material arises, the greater piezoelectric response is observed.

On the basis of the understanding formulated for the fluorocarbonates synthesized in this work and the fact that the SAMD metric provides a meaningful way to measure the deviation from centricity for structures with different cell volumes, we now explore the correlations between the countercations (alkaline) and central metal sites in the broader family of known 3D alkaline metal fluorcarbonates, including those reported elsewhere (see Table 2). Figure 8 shows the variance in the metal ionic radii positively correlates with the SAMD in $A^{1+}M^{2+}$ fluorocarbonates, which cluster into two distinct groups indicated by filled circles (red symbols) and squares (blue symbols). The best linear fit to the data (gray line) gives a cross-correlation coefficient of 0.82, indicating that the ionic radii size mismatch between the alkali and divalent cations provides a reasonable measure of the acentricity of the structure. As the cation variance increases, the amplitude of the inversion breaking distortions increase (SAMD becomes larger), which is indicative of an enhanced structural contribution to the SHG response.[61] Above a value of approximately 0.07 Å^2, which separates the fluorocarbonate compounds into two clusters, a unit cell tripling is observed. The volume change coincides with the crossover from a carbonate topology with fully aligned triangular moieties to one with rotated and antialigned triangular units (Figure 8, inset). Note that the $RbPbCO_3F$ and $CsPbCO_3F$ compounds synthesized in this work are found below that transition region with the two largest SAMD values in the fluorocarbonate grouping distinguished by fully aligned $[CO_3]^{2-}$ triangles.

A simplistic view of this correlation suggests that the NLO response should increase with the value of the specific acentric-mode displacements. Figure 8b shows the experimentally measured SHG intensity relative to that of KDP with respect to the calculated SAMD values for each compound. The differentiation between the fluorocarbonates with Z = 1 and Z = 3 becomes increasingly apparent. Despite an increase in the SAMD value, the antialignment of the carbonate groups for Z = 3 $RbCaCO_3F$ and $CsCaCO_3F$ reduces the SHG response. *Thus, for achiral and nonpolar compounds, a large SAMD value does not guarantee that a large NLO response will result; the relative* *orientation of the displacements contributing to the mode-polarization amplitude need to be considered.* This becomes more evident if the acentric displacements used in the SAMD calculation are projected onto a plane of reduced symmetry, for example, the $(2\bar{1}0)$ plane corresponding to a vertex of the Reuleaux triangle along which the PbO_6F_2 exhibit *local* dipoles, as a way to separate the contributions to SAMD from those acentric distortions that occur because of the change in translational symmetry. For structures with $Z = 1$ and space group $P\bar{6}m2$, this coincides with a mirror plane that is absent in the $Z = 3$ $P\bar{6}2m$ structures. Figure 8c shows that the reduced quantity obtained in that plane, SAMD$|(2\bar{1}0)$, is less than the full value of the SAMD, because it provides a measure of the local acentric displacements relative to these crystal symmetries rather than the cooperative effect. Thus, while the $RbCaCO_3F$ and $CsCaCO_3F$ structures appear to be more distorted relative to those fluorocarbonates synthesized here (Figure 8a), that is, the large SAMD value derives largely from the rotations of the carbonate groups that lead to the antialignment and cell tripling distortion, the additive nature of the acentric moieties leads to a net reduction in SHG. Indeed, a least-squares linear fit of the reduced acentricity descriptor (Figure 8c), which only considers such displacements relative to directions of symmetries that generate enantiomorphic pairs, is positively correlated with the experimental SHG intensity ($R = 0.94$). The analysis of local displacements relative to inversion generating operations is important when explaining the SHG efficiency of nonpolar but noncentrosymmetric crystal structures and it provides an intuitive way to understand the relationships between acentric physical properties and missing symmetry elements.

■ CONCLUSIONS

We synthesized and characterized two acentric alkali-metal lead fluorocarbonates, namely, $RbPbCO_3F$ and $CsPbCO_3F$. Both materials exhibit achiral and nonpolar noncentrosymmetric 3D structures. Powder SHG measurements revealed efficiencies of approximately 250 and 300 × α-SiO_2 with d_{33} piezoelectric charge constants of approximately 72 and 94 pm/V for $RbPbCO_3F$ and $CsPbCO_3F$, respectively. SAMD analyses reveal that the nonlinear optical response is derived from the locally polar PbO_6F_2 units and the cooperatively aligned triangular carbonate units. Importantly, we find that large inversion symmetry lifting distortions, i.e. large SAMD values, which sum to form the mode-polarization amplitude, do not guarantee a large SHG response; the relative orientation of the displacements contributing to the mode-polarization amplitude need to be taken into account when discussing acentric structure−property relationships especially for achiral and nonpolar acentric structures. By examining the anisotropy in the charge distribution and dynamical charges, we identified key directions of reduced symmetry in the fluorocarbonate crystal structures that provide a positive correlation between the amplitude of the atomic displacements and the SHG. This analysis enabled a quantitative assessment and atomic scale explanation of the origin of the enhanced frequency doubling in $CsPbCO_3F$ compared to $RbPbCO_3F$. We plan to explore the generality of this conclusion in a variety of acentric materials beyond fluorocarbonates, with structures crystallizing in polar, nonpolar, chiral, and achiral symmetries.

■ ASSOCIATED CONTENT

Ⓢ Supporting Information

X-ray crystallographic file in CIF format, experimental and calculated powder X-ray diffraction patterns, infrared and UV−vis spectra, thermogravimetric and differential thermal analysis diagrams, electron localization function (ELF) and isosurfaces, select bond distances and angles, atomic coordinates, detailed bond valence calculation tables and ideal $P\bar{6}m2$ structure used in the mode-polarization vector analyses. This material is available free of charge via the Internet at http://pubs.acs.org.

■ AUTHOR INFORMATION

Corresponding Authors

*E-mail: psh@uh.edu. (P.S.H.)
*E-mail: jrondinelli@coe.drexel.edu. (J.M.R.)

Notes

The authors declare no competing financial interest.

■ ACKNOWLEDGMENTS

We thank Prof. Kenneth Poeppelmeier and Martin Donakowski for assistance in FTIR (at IMSERC at Northwestern University, which is supported with grants from NSF-NSEC, NSF-MRSEC, the Keck Foundation, the State of Illinois, and NU) and UV−vis reflectance measurements (at the Keck Biophysics Facility at Northwestern University, which is supported by grants from the W. M. Keck Foundation, NU, the National Institutes of Health, the Rice Foundation, and the Robert H. Lurie Comprehensive Cancer center). We would like to thank the United States Department of Energy−Basic Energy Sciences (DE-SC0005032) and the Welch Foundation (Grant E-1457) for support. J.M.R. acknowledges support from the American Chemical Society Petroleum Research Fund (52138-DNI10) and computational resources provided by the Drexel University Research Computing Facility (URCF). T.T.T. thanks the Ludo Frevel Crystallography Scholarship 2014 for support.

■ REFERENCES

(1) Lu, H.; Gautier, R.; Donakowski, M. D.; Tran, T. T.; Edwards, B. W.; Nino, J. C.; Halasyamani, P. S.; Liu, Z.; Poeppelmeier, K. R. *J. Am. Chem. Soc.* **2013**, *135*, 11942.

(2) Zhang, M.; Pan, S.; Yang, Z.; Wang, Y.; Su, X.; Yang, Y.; Huang, Z.; Han, S.; Poeppelmeier, K. R. *J. Mater. Chem. C* **2013**, *1*, 4740.

(3) Huang, H.; He, R.; Yao, W.; Lin, Z.; Chen, C.; Zhang, Y. *J. Cryst. Growth* **2013**, *380*, 176.

(4) Matyjasik, S.; Shaldin, Y. V. *Low Temp. Phys.* **2013**, *39*, 967.

(5) Kesim, M. T.; Zhang, J.; Trolier-McKinstry, S.; Mantese, J. V.; Whatmore, R. W.; Alpay, S. P. *J. Appl. Phys.* **2013**, *114*, 204101/1.

(6) Luo, K.; Johnson, R. D.; Tran, T. T.; Halasyamani, P. S.; Radaelli, P. G.; Hayward, M. A. *Chem. Mater.* **2013**, *25*, 1800.

(7) Padhee, R.; Das, P. R.; Parida, B. N.; Choudhary, R. N. P. *J. Electron. Mater.* **2013**, *42*, 426.

(8) Pandey, R.; Meena, B. R.; Singh, A. K. *Condens. Matter* **2013**, 1.

(9) Freitas, V. F.; Protzek, O. A.; Montoro, L. A.; Goncalves, A. M.; Garcia, D.; Eiras, J. A.; Guo, R.; Bhalla, A. S.; Cotica, L. F.; Santos, I. A. *J. Mater. Chem. C* **2014**, *2*, 364.

(10) Gautier, R.; Norquist, A. J.; Poeppelmeier, K. R. *Cryst. Growth Des.* **2012**, *12*, 6267.

(11) Wu, H.; Yu, H.; Yang, Z.; Hou, X.; Su, X.; Pan, S.; Poeppelmeier, K. R.; Rondinelli, J. M. *J. Am. Chem. Soc.* **2013**, *135*, 4215.

(12) Zhang, G.; Li, Y.; Jiang, K.; Zeng, H.; Liu, T.; Chen, X.; Qin, J.; Lin, Z.; Fu, P.; Wu, Y.; Chen, C. *J. Am. Chem. Soc.* **2012**, *134*, 14818.

(13) Yan, X.; Luo, S.; Lin, Z.; Yue, Y.; Wang, X.; Liu, L.; Chen, C. *J. Mater. Chem. C* **2013**, *1*, 3616.

(14) Wu, H.; Pan, S.; Poeppelmeier, K. R.; Li, H.; Jia, D.; Chen, Z.; Fan, X.; Yang, Y.; Rondinelli, J. M.; Luo, H. *J. Am. Chem. Soc.* **2011**, *133*, 7786.

(15) Young, J.; Rondinelli, J. M. *Chem. Mater.* **2013**, *25*, 4545.

(16) Gou, G.; Rondinelli, J. M. *Condens. Matter* **2013**, 1.

(17) Mulder, A. T.; Benedek, N. A.; Rondinelli, J. M.; Fennie, C. J. *Adv. Funct. Mater.* **2013**, *23*, 4810.

(18) Fry, A. M.; Seibel, H. A.; Lokuhewa, I. N.; Woodward, P. M. *J. Am. Chem. Soc.* **2012**, *134*, 2621.

(19) Fry, A. M.; Woodward, P. M. *Cryst. Growth Des.* **2013**, *13*, 5404.

(20) Turp, S. A.; Hargreaves, J.; Baek, J.; Halasyamani, P. S.; Hayward, M. A. *Chem. Mater.* **2010**, *22*, 5580.

(21) Benedek, N. A.; Fennie, C. J. *J. Phys. Chem. C* **2013**, *117*, 13339.

(22) Benedek, N. A.; Mulder, A. T.; Fennie, C. J. *J. Solid State Chem.* **2012**, *195*, 11.

(23) Ke, X.; Birol, T.; Misra, R.; Lee, J. H.; Kirby, B. J.; Schlom, D. G.; Fennie, C. J.; Freeland, J. W. *Phys. Rev. B: Condens. Matter Mater. Phys.* **2013**, *88*, 094434/1.

(24) Olshansky, J. H.; Thao, T. T.; Hernandez, K. J.; Zeller, M.; Halasyamani, P. S.; Schrier, J.; Norquist, A. J. *Inorg. Chem.* **2012**, *51*, 11040.

(25) Koffer, J. H.; Olshansky, J. H.; Smith, M. D.; Hernandez, K. J.; Zeller, M.; Ferrence, G. M.; Schrier, J.; Norquist, A. J. *Cryst. Growth Des.* **2013**, *13*, 4504.

(26) Yang, B.-P.; Hu, C.-L.; Xu, X.; Huang, C.; Mao, J.-G. *Inorg. Chem.* **2013**, *52*, 5378.

(27) Huang, C.; Hu, C.-L.; Xu, X.; Yang, B.-P.; Mao, J.-G. *Dalton Trans.* **2013**, *42*, 7051.

(28) Song, J.-L.; Hu, C.-L.; Xu, X.; Kong, F.; Mao, J.-G. *Inorg. Chem.* **2013**, *52*, 8979.

(29) Huang, C.; Hu, C.-L.; Xu, X.; Yang, B.-P.; Mao, J.-G. *Inorg. Chem.* **2013**, *52*, 11551.

(30) Meier, D.; Lilienblum, M.; Becker, P.; Bohaty, L.; Spaldin, N. A.; Ramesh, R.; Fiebig, M. *Phase Transitions* **2013**, *86*, 33.

(31) Artyukhin, S.; Delaney, K. T.; Spaldin, N. A.; Mostovoy, M. *Nat. Mater.* **2013**, *13*, 8.

(32) Garcia-Castro, A. C.; Spaldin, N. A.; Romero, A. H.; Bousquet, E. *Condens. Matter* **2013**, 1.

(33) Inaguma, Y.; Aimi, A.; Shirako, Y.; Sakurai, D.; Mori, D.; Kojitani, H.; Akaogi, M.; Nakayama, M. *J. Am. Chem. Soc.* **2014**, *136*, 2748.

(34) Taniguchi, H.; Kuwabara, A.; Kim, J.; Kim, Y.; Moriwake, H.; Kim, S.; Hoshiyama, T.; Koyama, T.; Mori, S.; Takata, M.; Hosono, H.; Inaguma, Y.; Itoh, M. *Angew. Chem., Int. Ed.* **2013**, *52*, 8088.

(35) Inaguma, Y.; Sakurai, D.; Aimi, A.; Yoshida, M.; Katsumata, T.; Mori, D.; Yeon, J.; Halasyamani, P. S. *J. Solid State Chem.* **2012**, *195*, 115.

(36) Nguyen, S. D.; Yeon, J.; Kim, S.-H.; Halasyamani, P. S. *J. Am. Chem. Soc.* **2011**, *133*, 12422.

(37) Nguyen, S. D.; Kim, S.-H.; Halasyamani, P. S. *Inorg. Chem.* **2011**, *50*, 5215.

(38) Yeon, J.; Kim, S.-H.; Nguyen, S. D.; Lee, H.; Halasyamani, P. S. *Inorg. Chem.* **2012**, *51*, 609.

(39) Yeon, J.; Kim, S.-H.; Nguyen, S. D.; Lee, H.; Halasyamani, P. S. *Inorg. Chem.* **2012**, *51*, 2662.

(40) Nguyen, S. D.; Halasyamani, P. S. *Inorg. Chem.* **2013**, *52*, 2637.

(41) Kim, S.-H.; Yeon, J.; Halasyamani, P. S. *Chem. Mater.* **2009**, *21*, 5335.

(42) Halasyamani, P. S. *Chem. Mater.* **2004**, *16*, 3586.

(43) Pachoud, E.; Zhang, W.; Tapp, J.; Liang, K.-C.; Lorenz, B.; Chu, P. C. W.; Halasyamani, P. S. *Cryst. Growth Des.* **2013**, *13*, 5473.

(44) Opik, U.; Pryce, M. H. L. *Proc. R. Soc. London, Ser. A* **1957**, *238*, 425.

(45) Pearson, R. G. *J. Mol. Struct.: THEOCHEM* **1983**, *12*, 25.

(46) Wheeler, R. A.; Whangbo, M. H.; Hughbanks, T.; Hoffmann, R.; Burdett, J. K.; Albright, T. A. *J. Am. Chem. Soc.* **1986**, *108*, 2222.

(47) Goodenough, J. B. *Annu. Rev. Mater. Sci.* **1998**, *28*, 1.

(48) Ye, N.; Chen, Q.; Wu, B.; Chen, C. *J. Appl. Phys.* **1998**, *84*, 555.

(49) Grice, J. D.; Maisonneuve, V.; Leblanc, M. *Chem. Rev.* **2007**, *107*, 114.

(50) Luo, M.; Ye, N.; Zou, G.; Lin, C.; Cheng, W. *Chem. Mater.* **2013**, *25*, 3147.

(51) Zou, G.; Ye, N.; Huang, L.; Lin, X. *J. Am. Chem. Soc.* **2011**, *133*, 20001.

(52) Ben, A. A.; Leblanc, M.; Maisonneuve, V. *Acta Crystallogr., Sect. E: Struct. Rep. Online* **2006**, *62*, i133.

(53) Ben, A. A.; Maisonneuve, V.; Leblanc, M. *Solid State Sci.* **2002**, *4*, 1367.

(54) Mercier, N.; Leblanc, M. *Acta Crystallogr., Sect. C: Cryst. Struct. Commun.* **1994**, *C50*, 1864.

(55) Mercier, N.; Taulelle, F.; Leblanc, M. *Eur. J. Solid State Inorg. Chem.* **1993**, *30*, 609.

(56) Mercier, N.; Leblanc, M. *Eur. J. Solid State Inorg. Chem.* **1993**, *30*, 217.

(57) Ben, A. A.; Maisonneuve, V.; Smiri, L. S.; Leblanc, M. *Solid State Sci.* **2002**, *4*, 891.

(58) Ben, A. A.; Maisonneuve, V.; Kodjikian, S.; Smiri, L. S.; Leblanc, M. *Solid State Sci.* **2002**, *4*, 503.

(59) Tran, T. T.; Halasyamani, P. S. *Inorg. Chem.* **2013**, *52*, 2466.

(60) Zou, G.; Huang, L.; Ye, N.; Lin, C.; Cheng, W.; Huang, H. *J. Am. Chem. Soc.* **2013**, *135*, 18560.

(61) Cammarata, A.; Rondinelli, J. M. *ACS Photonics* **2014**, *1*, 96.

(62) SAINT. In *Siemens Analytical X-ray Systems*, 4.05 ed.; Siemens, Inc.: Madison, WI, 1995.

(63) Sheldrick, G. M. SHELXS-97. In *Program for Solution of Crystal Structures;* University of Gottingen: Gottingen, Germany, 1997.

(64) Sheldrick, G. M. SHELXL-97. In *Program for Refinement of Crystal Structures;* University of Gottingen: Gottingen, Germany, 1997.

(65) Farrugia, L. J. *J. Appl. Crystallogr.* **1999**, *32*, 837.

(66) M.Kubelka, P.; Munk, F. Z. *Tech. Phys.* **1931**, *12*, 593.

(67) Tauc, J. *Mater. Res. Bull.* **1970**, *5*, 721.

(68) Ok, K. M.; Chi, E. O.; Halasyamani, P. S. *Chem. Soc. Rev.* **2006**, *35*, 710.

(69) Kurtz, S. K.; Perry, T. T. *J. Appl. Phys.* **1968**, *39*, 3798.

(70) Momma, K.; Izumi, F. *J. Appl. Crystallogr.* **2011**, *44*, 1272.

(71) Kresse, G.; Hafner, J. *Phys. Rev. B: Condens. Matter* **1993**, *47*, 558.

(72) Kresse, G.; Furthmüller, J. *Comput. Mater. Sci.* **1996**, *6*, 15.

(73) Perdew, J. P.; Ruzsinszky, A.; Csonka, G. I.; Vydrov, O. A.; Scuseria, G. E.; Constantin, L. A.; Zhou, X.; Burke, K. *Phys. Rev. Lett.* **2008**, *100*, 136406/1.

(74) Bloechl, P. E. *Phys. Rev. B: Condens. Matter* **1994**, *50*, 17953.

(75) Blochl, P. E.; Jepsen, O.; Andersen, O. K. *Phys. Rev. B: Condens. Matter* **1994**, *49*, 16223.

(76) Brown, I. D.; Altermatt, D. *Acta Crystallogr., Sect. B: Struct. Sci.* **1985**, *B41*, 244.

(77) Brown, I. D. *The Chemical Bond in Inorganic Chemistry;* Oxford University Press: New York, 2002; Vol. *12*.

(78) Donoghue, M.; Hepburn, P. H.; Ross, S. D. *Spectrochimica Acta Part A: Molecular Spectroscopy* **1971**, *27*, 1065.

(79) Andersen, F. A.; Brecevic, L. *Acta Chem. Scand.* **1991**, *45*, 1018.

(80) Refat, M. S.; Elsabawy, K. M. *Bull. Mater. Sci.* **2011**, *34*, 873.

(81) Nakamoto, K. *Infrared and Raman Spectra of Inorganic and Coordination Compounds;* Wiley: Hoboken, NJ; Chichester, U.K., 2007.

(82) Oka, K.; Unoki, H.; Sakudo, T. *J. Cryst. Growth* **1979**, *47*, 568.

(83) Kurtz, S. K.; Perry, T. T. *J. Appl. Phys.* **1968**, *39*, 3798.

(84) Kampf, A. R.; Yang, H.; Downs, R. T.; Pinch, W. W. *Am. Mineral.* **2011**, *96*, 402.

(85) Marukhnov, A. V.; Pushkin, D. V.; Serezhkin, V. N. *Russ. J. Coord. Chem.* **2008**, *34*, 570.

(86) Shannon, R. D. *Acta Crystallogr., Sect. A* **1976**, *A32*, 751.

(87) Grice, J. D.; Van, V. J.; Gault, R. A. *Can. Mineral.* **1994**, *32*, 405.

(88) Grice, J. D.; Gault, A.; Van, V. J. *Can. Mineral.* **1997**, *35*, 181.

(89) Grice, J. D.; Chao, G. Y. *Am. Mineral.* **1997**, *82*, 1255.

(90) Griffiths, D.; Culpin, D. *Mathl. Gaz.* **1975**, *59*, 165.

(91) Xu, Y. *Ferroelectric Materials and Their Applications;* Elsevier Science Publishers: Amsterdam, 1991.

(92) Fukunaga, M.; Uesu, Y. *Jpn. J. Appl. Phys., Part 1* **2003**, *42*, 6115.

(93) Roy, A. K.; Prasad, K.; Prasad, A. *Process. Appl. Ceram.* **2013**, *7*, 81.

(94) Piilonen, P. C.; McDonald, A. M.; Grice, J. D.; Cooper, M. A.; Kolitsch, U.; Rowe, R.; Gault, R. A.; Poirier, G. *Mineral. Mag.* **2010**, *74*, 257.

(95) Grice, J. D.; Chao, G. Y. *Can. Mineral.* **1997**, *35*, 743.

(96) Mercier, N.; Leblanc, M.; Antic-Fidancev, E.; Lemaitre-Blaise, M.; Porcher, P. *J. Alloys Compd.* **1995**, *225*, 198.

(97) Mercier, N.; Leblanc, M.; Durand, J. *Eur. J. Solid State Inorg. Chem.* **1997**, *34*, 241.

(98) Mercier, N.; Leblanc, M. *Eur. J. Solid State Inorg. Chem.* **1994**, *31*, 423.